# Dynamical and Microphysical Retrievals from Doppler Radar Observations of a Deep Convective Cloud

BING WU AND JOHANNES VERLINDE

*Department of Meteorology, The Pennsylvania State University, University Park, Pennsylvania*

JUANZHEN SUN

*National Center for Atmospheric Research, Boulder, Colorado*

ABSTRACT

A four-dimensional variational data assimilation system consisting of a three-dimensional time-dependent cloud model with both liquid and ice phase microphysics parameterization was used to assimilate radar data into a cloud model. Data of a severe thunderstorm observed during the Cooperative Huntsville Meteorological Experiment project were assimilated and results compared to a conventional analysis. The analysis system was able to retrieve all the prominent features of the storm, but differed in some of the details. However, the consistency of this retrieval dataset lent credence to the results.

It was found that the algorithm was very sensitive to several coefficients in the microphysical and turbulence parameterizations. Simulations proved to be unable to reproduce the evolution of the observed storm even with parameterization coefficients set at values that produce reasonable storm evolutions. This result has implications for short-range forecasting of convective events. Such forecasts require initial fields that currently can only be derived from observations such as used in this study. The problems with assimilating radar observations point to additional work to design parameterizations that allow models to more accurately simulate actual observed storms.

## 1. Introduction

One of the principal observational tools for the study of precipitating clouds is the Doppler radar. State-of-the-art Doppler radars can rapidly scan through cloud systems, thereby acquiring observations in all parts of the cloud. By repeating the scan sequence, an evolution of the cloud development may be constructed. These Doppler radars measure the velocity component along the beam, and total backscattered power from the hydrometeors. With the development of radar technology, new measurements with more information content about the hydrometeor characteristics are becoming available. These measurements are being made by exploiting different polarization states of the transmitted and received signals.

Different approaches have been used to study convective clouds, such as numerical models, Doppler and in situ observations, and laboratory work. With advances in the understanding of cloud systems, observational systems, and computer technology, the time is right to combine these (typically) separate approaches into a single comprehensive system. Such an analysis system would provide the means to derive the unobserved wind, thermal, and microphysical fields from Doppler radar (and other) observations. These derived fields are determined in a dynamically consistent way by obtaining an optimal fit of a numerical model to a set of observations, and as such, provide a useful tool to study convective precipitating storms. Moreover, with the continual push toward finer-resolution numerical prediction models, it is necessary that analysis tools be developed to provide initial fields for those forecast models. The only current existing facilities that do provide such observations are the National Weather Service Doppler radars, pointing to the need to convert radar measurements into typical model-predicted variables.

Gal-Chen (1978) presented the first results using an anelastic model to retrieve pressure and thermodynamic values from sets of dual-Doppler analyses. With increases in computing power, the focus shifted to full four-dimensional variational (4DVAR) data assimilation (Lewis and Derber 1985; Talagrand and Courtier 1987). Two distinct approaches were followed applying 4DVAR to the assimilation of radar data. The simplest

*Corresponding author address:* Dr. Hans Verlinde, Department of Meteorology, 503 Walker Building, The Pennsylvania State University, University Park, PA 16802-5013.
E-mail: verlinde@essc.psu.edu

approach relied on time-dependent conservation equations for reflectivity and/or velocity (Qiu and Xu 1992; Laroche and Zawadzki 1994; Shapiro et al. 1995), while the second employed time-dependent dynamical models (Wolfsberg 1987; Kapitza 1991; Sun et al. 1991) or microphysical models (Verlinde and Cotton 1993). More recently, microphysical processes have been added to the dynamical models (Sun and Crook 1997, hereafter SC97; Sun and Crook 1998, hereafter SC98). In these studies an anelastic cloud model and its adjoint were used to retrieve the wind, temperature, pressure, and microphysical fields in moist convective systems from single- or multiple-Doppler radar observations. These studies were restricted to shallow convective storms containing only liquid physics. However, most thunderstorms are influenced by ice phase physics. Therefore, the technique must be tested on clouds where ice phase physics is important.

In this paper we extend the application of the SC97 model to deep convective storms where the ice phase plays an important role. The algorithm is tested using an observational dataset collected in the Cooperative Huntsville Meteorological Experiment (COHMEX) (Dodge et al. 1986). On 20 July 1986 almost the entire life cycle of an isolated, microburst-producing cumulonimbus cloud was documented by three Doppler radars, one of which had polarimetric abilities. These data have been analyzed by Wakimoto and Bringi (1988), Tuttle et al. (1989), and Kingsmill and Wakimoto (1991, hereafter KW91). In addition, Proctor (1989) and Straka and Anderson (1993) have performed numerical investigations of the same system. These studies provide a basis for evaluating our retrieval results.

Several studies have shown that different polarimetric variables can be used to identify hydrometeor characteristics in clouds (i.e., Vivekanandan et al. 1993; Bringi and Hendry 1990; Jameson and Johnson 1990; Brandes et al. 1995; Seliga et al. 1986). This paper reports on an initial attempt to use differential reflectivity ($Z_{DR}$, the ratio of the horizontally polarized backscattered power to the vertically polarized backscattered power) to improve on the retrieval of microphysical information in mixed-phase conditions, in particular, to discriminate between the contribution of hail and rain to the radar reflectivity.

## 2. Microphysics

Reports of pea-sized hail, radar reflectivities over 60 dBZ, and differential reflectivities ($Z_{DR}$) close to zero (Tuttle et al. 1989) all indicate the presence of hail in the 20 July 1986 storm. Since the evolution of any convective cloud is the result of interaction between its dynamical and microphysical processes, it is necessary to adequately represent the important contributions of both if one is to model accurately the evolution of the storm. Straka and Anderson (1993) investigated the effects of including the ice phase in numerical simulations

of the 20 July and other COHMEX storms. They reported differences between simulations with and without the ice phase. The biggest differences were found in the strengths of the vertical velocity fields, with maximum updrafts 10%–30% stronger, and low-level downdrafts (the microburst) twice as strong in some cases with ice included. These results indicate that the ice phase played an important role in some of the dominant features of the 20 July storm and, therefore, that any system seeking to assimilate the observed radar data would need to include the ice phase.

We have chosen the SC97 model as the basis for our work. Since this model only includes liquid phase physics, its microphysics parameterization had to be expanded to include the ice phase. However, the inclusion of the ice phase greatly increases the complexity of the microphysics parameterization. This complexity is a result of the many possible categories of ice hydrometeors, and also of the variety of shapes that may exist within each category. Therefore, we had to make many simplifications. Generally, the most complete bulk parameterization models include ice categories for cloud ice (individual crystals), snow (aggregates), and graupel and/or hail (graupel/hail). However, such a model will have a complex adjoint model with poor convergence properties in its assimilation applications, resulting from many nonlinearities. Therefore, we sought to develop a simple yet efficient way to parameterize the ice phase microphysics in our model, whereby we would maintain the ability to simulate accurately the dynamical and microphysical evolution of the storm. This would allow us to fit both the model-calculated velocities and reflectivities to the observations. This simplification was accomplished by using a scheme without the snow category, and merged cloud water–cloud ice categories.

The microphysics scheme used in this study therefore consists of three categories: rain, hail, and a cloud liquid–ice category (Fig. 1). The original parameterization of SC97 included rain and cloud and allowed for the following microphysical processes: condensation and evaporation of cloud water (implicit in the thermodynamic variable liquid potential temperature), accretion of cloud liquid by rain, autoconversion of cloud liquid to rain, evaporation of raindrops in subsaturated air, and sedimentation of rain. With the addition of a single ice category (graupel/hail), one additional prognostic equation (for hail) was added to the SC97 scheme. Associated with the ice category, we implemented several additional processes (see appendix A for details): the freezing of raindrops, collection of raindrops by hail, accretion of cloud liquid by hail, melting of hail, and precipitation of hail.

Even though the scheme is rather simple, its use can be justified. Hauser et al. (1988) used a similar scheme in their kinematic microphysical retrieval model. They were able to retrieve microphysical fields that yielded good comparisons with the observed reflectivity fields (which in their case were independent fields, not used in the assimilation). Lin et al. (1983), using a cloud
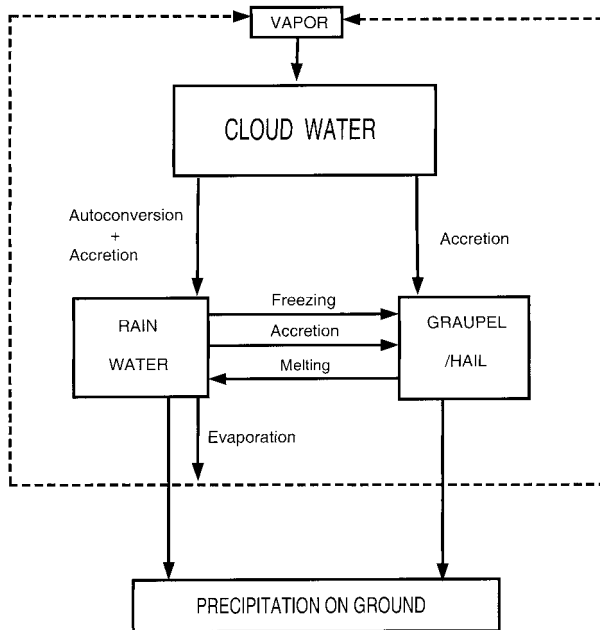
FIG. 1. A schematic of the microphysical categories and processes implemented in the model.

model with a very detailed ice phase parameterization, reported that the impact of including snow in a convective storm was to reduce the amount of rain produced early in the life history of the cloud and also to reduce the number of ice crystals for the entire life of the cloud. The reduction in rain was associated with a faster production of hail via rain–snow collisions early in the process, but the reduction in rain was small compared to the total amount of rain produced during the life cycle of the cloud. Similarly, the conversion of ice to snow has little impact on the thermodynamics of the storm, since no phase change is involved and both categories have similar fall speeds. In addition, Straka and Anderson (1993), using another bulk parameterization, reported similar results for a numerical simulation of same thunderstorm we are studying. They found that the largest sources of rain were melting of hail and accretion of cloud liquid by rain, while the largest sources of hail were accretion of cloud liquid by hail, and freezing of rain. The effects of melting and sublimation of snow were very small compared to that of melting of graupel/hail and evaporation of rain.

Since hail in the radar volume increases the reflectivity, reflectivity versus rainwater mixing ratio ($Z_e$–$q_r$) relationships as used by SC97 will tend to overestimate the rainwater content in the cloud. However, this problem can be alleviated by using measurements of $Z_{DR}$. In principle, $Z_{DR}$ measurements allow for discrimination between rain and hail water content (see appendix A) and thus provide an independent source of information. This additional information allows the use of phase-dependent reflectivity–mixing ratio relationships.

## 3. Experiments defined

The objective of the 4DVAR system is to find an initial state that can, upon model integration, produce output parameters matching the radar observation as closely as possible. This 4DVAR system consists of a forward integration model and an adjoint model. The "goodness" of fit is defined by a scalar cost function, the value of which is the square of the differences between the modeled and observed radial velocities and hydrometeor mixing ratios. Some additional constraints have been added, following SC97. This cost function is minimized by adjusting the initial conditions to an "optimal" state. This optimal state is determined by an iterative procedure. The value of the cost function is calculated during a forward integration by comparing model-predicted values to the actual measurements (in time and space). The gradient of the cost function with respect to the initial conditions is computed through integration of the adjoint model. The initial conditions are then adjusted using the calculated gradient, and the process is repeated until the cost function is minimized. Nocedal's limited memory, quasi-Newton conjugate gradient method (Liu and Nocedal 1989) has been used as the minimization algorithm in this study. More detailed discussion on the adjoint model and minimization algorithms implemented in our model can be seen in Sun et al. (1991) and Sun and Crook (1994).

Variational techniques produce optimal results when the function being fitted is continuous and smooth. With each addition to the model physics, new discontinuities are added; it is therefore necessary to reevaluate the ability of the system to perform the task it is designed to do. This evaluation was accomplished by performing a series of observing system simulation experiments (OSSEs). In particular, it was necessary to see if the added discontinuities introduced in the model formulation would still permit the optimization routine to converge to the real solution in a reasonable number of iterations. Furthermore, these experiments allowed for a direct comparison with the work of SC97.

The model domain used for the OSSEs was $15 \times 15 \times 8.75$ km$^3$. The grid spacing was 600 m in the horizontal and 350 m in the vertical. The time step of the model integration was 7 s. The sounding used in these experiments (Fig. 2) was chosen with the purpose in mind to produce a shallow, mixed-phase cloud. The cloud for the control experiment was initiated by a warm, moist bubble inserted in the center of the domain at a height of 1750 m (above ground). The initial pulse was 10 km wide and 2 km deep, with a temperature excess of 1 K and a moisture excess of 1.2 g kg$^{-1}$. Simulated radar observations were created in a manner consistent with the scanning sequence of the three Doppler radars deployed during the COHMEX project. The simulated radial velocity and hydrometeor content (as opposed to reflectivity) were recorded at a radar-illuminated grid cell whenever its calculated radar re-
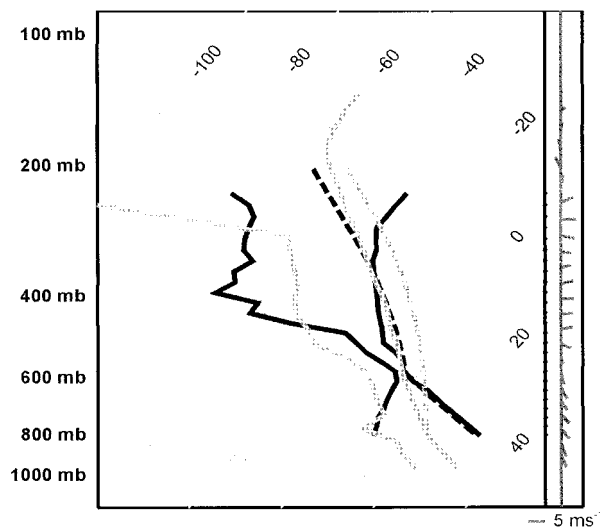
FIG. 2. Soundings used for OSSE (dark lines) and assimilation (lighter lines) experiments. The OSSE sounding is slightly modified from Sun and Crook (1997), while the assimilation sounding is the 20 July 1986 1200 CST sounding, released from the Redstone site approximately one hour before the radar observations of the storm.



FIG. 3. Relative position of radars and sounding site to the model domain.

flectivity value exceeded −10 dBZ (this value is close to the detectability of the radars involved).

The model domain was adjusted to 15 × 15 × 15 km³ for the assimilation of the 20 July observations. The increased vertical extent was necessary in order to accommodate the observed cloud-top height of the storm. It was accomplished by increasing the vertical resolution to 600 m. The sounding used in this experiment (Fig. 2) was released from the Redstone site (Fig. 3) approximately one hour before the storm formed.

In conventional multi-Doppler radar analysis it is assumed that a storm remains steady during the period required by all the radars to complete a single volume scan. The storm advection velocity is then used to advect individual measurements to a common time (Fig. 4a). This approach was used by SC97 in their OSSEs, though in their assimilation of observations (SC98) the time sequence information was included. All the work reported in this paper is based on assimilating data at the time step to which they actually correspond, as opposed to assimilation of the whole radar volume at a fixed time step. Aside from the obvious benefits of this approach, such as the evolution of the storm being accounted for and problems with the advection being avoided, there is another advantage. The position of a storm with respect to the observing radars is frequently not conducive to good multi-Doppler analysis. However, since the radars scan independently, they are not sampling the same space in time. For example, the storm observed on 20 July 1986 occurred at a location where two of the radars had similar viewing angles (Fig. 3) and therefore had little information content in a conventional multiple-Doppler analysis beyond that of a single radar. However, since the range-height-indicator scan performed by CP4 was different from the plan-po-
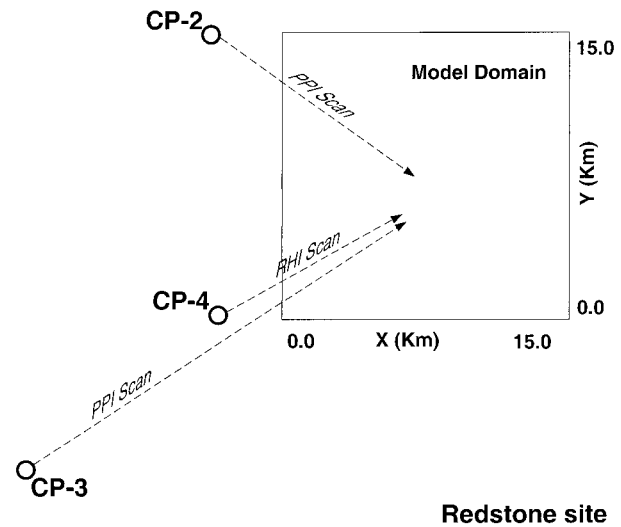
sition-indicator scan performed by CP3, the two radars scanned different places in the space–time domain.

Due to computer memory and time constraints, we were only able to assimilate two radar volume scans in one model run. The time period of two consecutive volume scans is defined as an assimilation period. Figure 4 shows how the radar observations in an assimilation period are inserted into the model. The thick dashed lines indicate the altitude scan sequences of the radar, and the thick solid lines in Figs. 4a,b represent the volume mean time (time when observations were inserted in model) for conventional dual-Doppler and steady-state evaluation experiments. Initial experiments were conducted in which only one volume scan of data was assimilated. However, it was found that details of cloud structure were missing. Considering that the smoothing and background penalties are only weak constraints in the model, one volume scan of radial velocity and reflectivity data might not be able to provide sufficient information to define a well-posed problem.

It is necessary to provide a complete model initiation to start each assimilation cycle. The model will converge to the correct solution only if the first guess of the initial fields are close to the correct solution; therefore, specification of this field is important. For assimilation experiments of the first two volumes, the initial guess (at time $t_0$ in Fig. 4) of vertical velocity values was set to zero, and the horizontal velocity fields were set to the environmental winds. The initial guess of mixing ratios of rain and ice was generated by projecting all the observations of rain and hail during the first volume scan onto the initial time of the assimilation period. The initial guess of total water mixing ratio and potential temperature was created as in SC97. For all subsequent assimilation periods, analyzed results (velocity and microphysics fields) from the middle of the previous as-
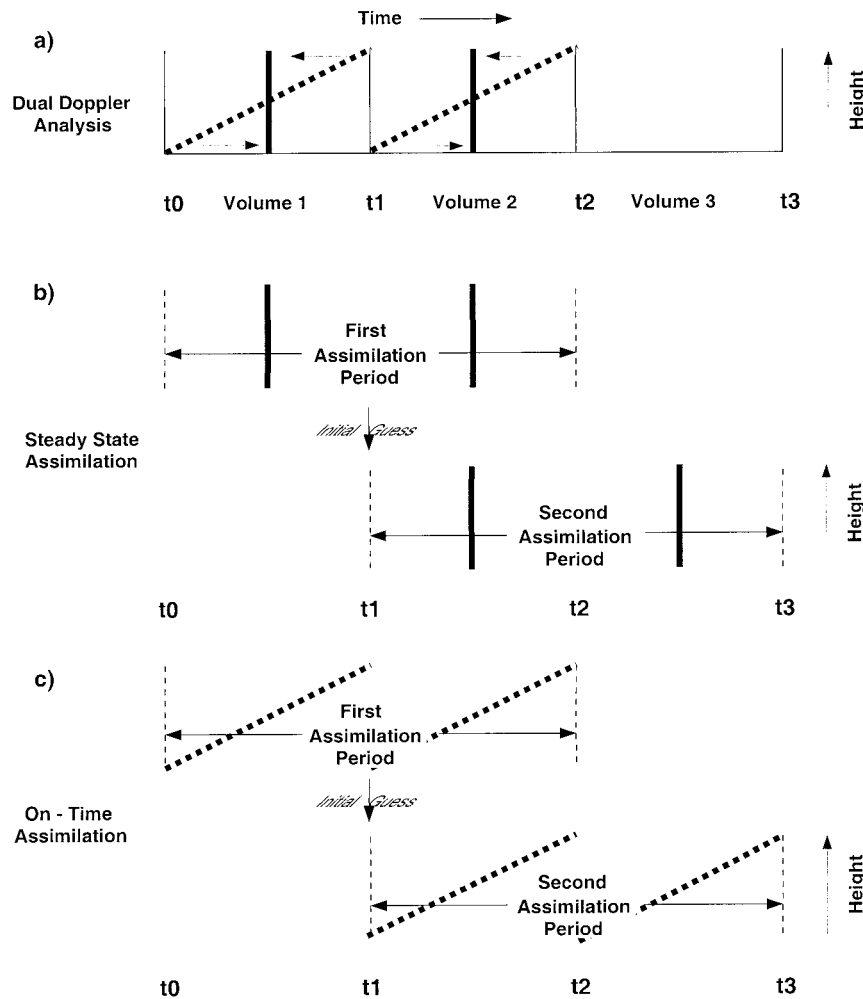
FIG. 4. Definition of assimilation period and the way the radar observations are inserted in the model: (a) dual-Doppler analysis, (b) steady-state assimilation, and (c) time sequence 4DVAR assimilation. The thick dashed lines indicate the altitude scan sequences of the radar; (a) and (b) thick solid lines represent the volume mean time (time when observations were inserted in model) for conventional dual-Doppler and steady-state evaluation experiments.

simlation period were used as the initial guess. For example, Fig. 4c shows that the initial guess for the second assimilation period is taken from the middle of the first assimilation period (at time $t_1$).

## 4. Observation System Simulation Experiments

The OSSEs were designed to test the model's ability to retrieve the microphysics and dynamics fields with the ice microphysics implemented in the model. In these experiments we sought to remain close to similar experiments conducted by SC97, but with two major differences: 1) ice microphysics have been included in the model; and 2) the simulated radar observations were created by using the exact relative locations and scanning patterns of the three Doppler radars deployed in the COHMEX project.

The cloud started to form in the simulation model at about 20 min, and the ice phase began to form after 25

min. The maximum rain mixing ratio and graupel/hail mixing ratio were 6 and 2 g kg$^{-1}$, respectively, while the maximum vertical velocity was 25 m s$^{-1}$. Simulated measurements were started 25 min into the simulation. Data from four volume scans, each 3 min long, were collected and used in the assimilation experiments. Figure 5 shows the horizontal velocity $u$, vertical velocity $w$, temperature perturbation $T$, total water mixing ratio $q_t$, rain mixing ratio $q_r$, and graupel/hail mixing ratio $q_h$ at 34 min for an $X$–$Z$ cross section through the center of the domain. The results of all the retrieval experiments are for this same time and cross section.

### a. Modifications to the microphysics in the model

Initial results from our OSSE revealed some problems in the algorithm. The retrieved microphysics fields were very noisy, and the minimization of the
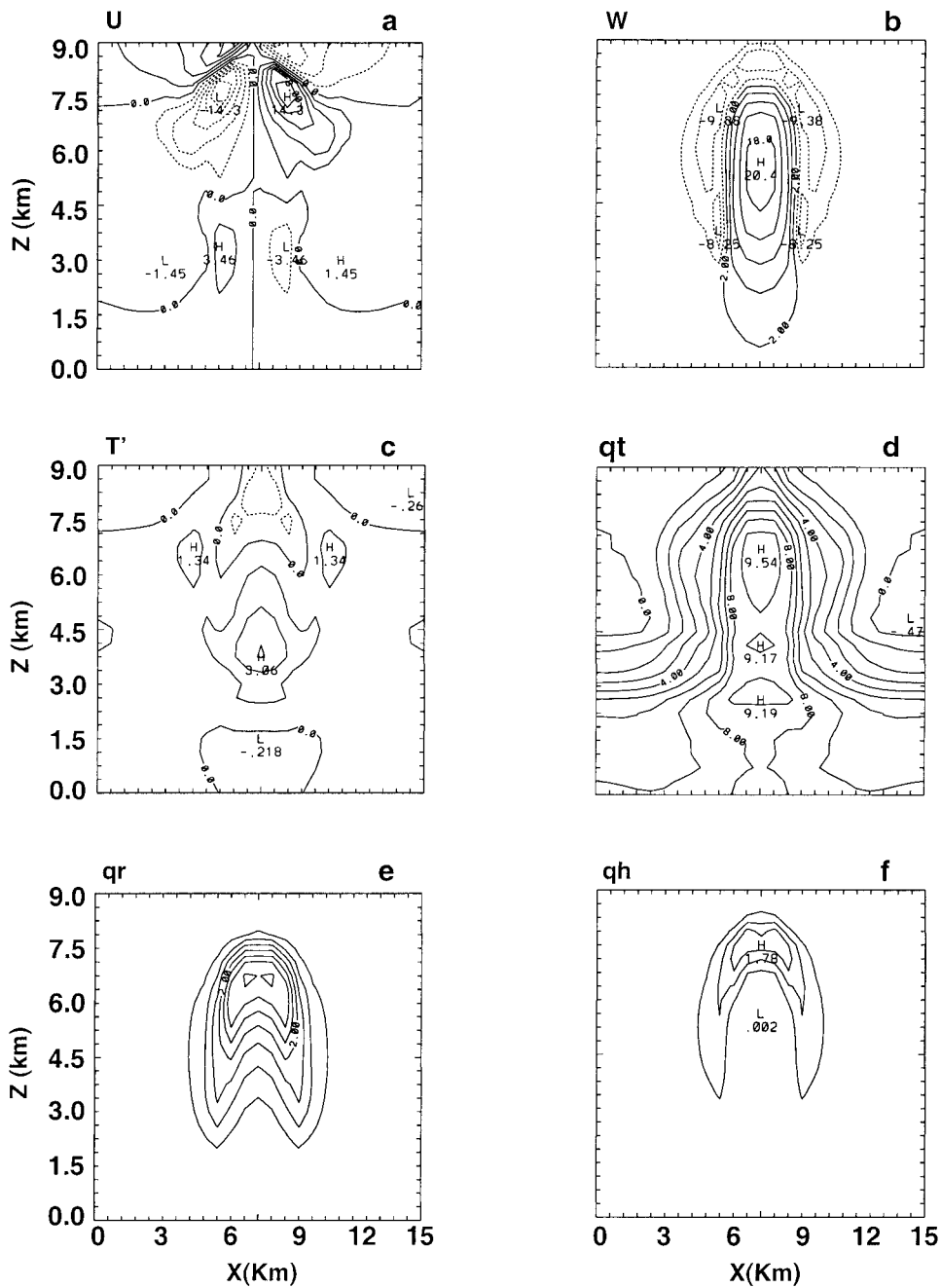
FIG. 5. Vertical cross sections through the center of the simulated storm at 34 min: (a) $x$ component of horizontal velocity in m s$^{-1}$ (contour interval 4 m s$^{-1}$); (b) vertical velocity in m s$^{-1}$ (contour interval 4 m s$^{-1}$); (c) temperature perturbation in °C (contour interval 1°C); (d) total water mixing ratio (contour interval 1 g kg$^{-1}$); (e) rainwater mixing ratio (contour interval 1 g kg$^{-1}$); and (f) graupel/hail mixing ratio (contour interval 1 g kg$^{-1}$).

cost function was not satisfactory. The cause of the problem was determined to be the calculation of the gradient associated with precipitation of very small values of rainwater and graupel/hail mixing ratio. SC97 reported similar difficulties with their model in association with evaporation and the terminal velocity of hydrometeors. They solved the problem by setting a

critical value of rain mixing ratio (0.05 g kg$^{-1}$), below which the evaporation rate and the terminal velocity are kept constant (with the value of the rain mixing ratio equal to 0.05 g kg$^{-1}$). In addition to these modifications suggested by SC97, we found it necessary to introduce another. The derivative of the precipitation term $[d/dz V_{Tm} q_i]$ is of the form

TABLE 1. The relative rms errors (rmse's) of our three experiments and the Sun and Crook (1997) experiment. The relative rmse is the rmse normalized by the standard deviation of the actual field. Here $U$ is the horizontal wind speed; $W$ the vertical velocity; $\theta_{il}$ the ice–liquid potential temperature; $T$ the actual temperature; and the rest of the variables the mixing ratios for the total water content, rain, hail, cloud water, and vapor, respectively.

| Exp | Model variables | | | | | | | | |
|---|---|---|---|---|---|---|---|---|---|
| | $U$ | $W$ | $\theta_{il}$ | $T$ | $q_t$ | $q_r$ | $q_h$ | $q_c$ | $q_v$ |
| Warm | 0.39 | 0.29 | 0.32 | 0.93 | 0.22 | 0.14 | N/A | 0.26 | 0.21 |
| Ice | 0.41 | 0.34 | 0.41 | 1.08 | 0.27 | 0.20 | 0.38 | 0.55 | 0.24 |
| Steady state | 0.63 | 0.58 | 0.54 | 1.29 | 0.31 | 0.21 | 0.51 | 0.64 | 0.26 |
| Sun and Crook | 0.002 | 0.003 | 0.002 | 0.45 | N/A | 0.007 | N/A | 0.01 | 0.002 |

$$\frac{\partial(V_{\mathrm{T}m}q_i)}{\partial q_i} = \mathrm{const} \times q_i^{0.125},$$

where $V_{\mathrm{T}m}$ is mass-weighted terminal velocity and $q_i$ can be either of the hydrometeor categories. When $q_i$ is very small, the difference between the values of the derivative is small because of the small exponent of $q_i$. Therefore, small values of $q_i$ will produce high values for the gradient. The impact of noise in the $q_i$ field was able to introduce sufficient noise into the calculation of the gradient to slow down the convergence. This problem was circumvented by setting a minimum criterion of 0.01 g kg$^{-1}$ for both hydrometeor classes. Implementation of the above reduced the noise in the retrieved microphysics fields and resulted in a further reduction in the cost function by almost an order of magnitude.

The correctness of the adjoint model was tested following Navon et al. (1992) by defining a function,

$$\Phi(\alpha) = \frac{F_n(x_0 + \alpha h) - F_n(x_0)}{\alpha \mathbf{G}_n \mathbf{h}},$$

where $F_n$ and $G_n$ represent the nonlinear model and tangent linear model operators, respectively, $\mathbf{h}$ is a normalized random vector operated on by $\mathbf{G}_n$, and $\alpha$ is a scalar. With the modified mixed-phase microphysics implemented in the model, the values of $\Phi$ were within

the bounds (0.999–1.006) for $\alpha$ varying from $10^{-2}$ to $10^{-12}$, indicating that the adjoint code is consistent with the forward model.

### b. OSSE assimilation experiments

Three sets of assimilation experiments have been performed. The quality of the three assimilation experiments is determined by the relative rms errors of the retrieved dynamics and microphysics fields. The relative rms error is the rms error normalized by the standard deviation of the actual field.

The first experiments were conducted to investigate how much impact the addition of the ice microphysics had on the assimilation system. Two OSSEs were done: one with only warm microphysics (duplicating the SC97 case, but with considerably less simulated observations); the other with the complete microphysical package, including the ice physics. This was followed by an experiment to evaluate the impact of the steady-state assumption on retrievals. We will report on each individually with the results summarized in Table 1.

#### 1) LIQUID PHASE PHYSICS

In this experiment, the model with only liquid phase physics has been used to test the ability of the model to retrieve the dynamical and microphysical fields. The thin lines in Fig. 6 show the decline of the normalized cost function and gradient norm as a function of iteration number. The normalized cost function is a measure of the goodness of fit of the model to the data and, with the gradient norm, indicates convergence properties. The value of both these functions should initially decline steeply and then flatten out as the model converges to the solution. The gradient norm shows a pattern of large fluctuations as it approaches the minimum. These fluctuations are associated with the discontinuous microphysical processes in the model. No attempts have been made to circumvent the discontinuities as suggested by Verlinde and Cotton (1993) or Xu (1996).

The relative rms errors are presented in the first row in Table 1. In comparing these errors with those of SC97 (the fourth row in Table 1), it can be noted that our errors are much larger (but still comparable to typical error in dual-Doppler analyses). However, the quanti-
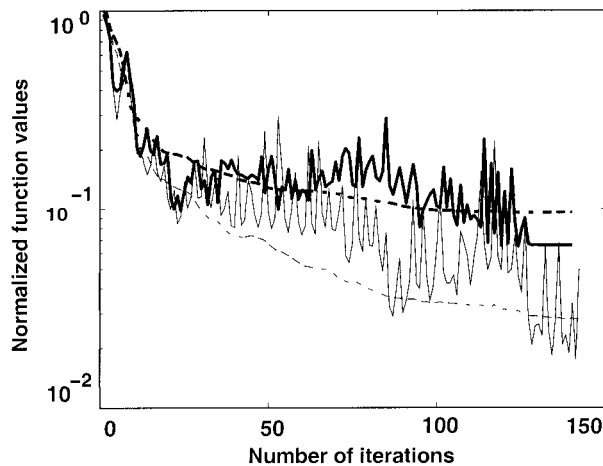


FIG. 6. Cost function (dashed lines) and gradient norm (solid lines). Thick lines represent results from model with ice microphysics. Thin lines represent results from model with only warm microphysics.

tative features of the storm are recovered well. These higher errors are attributed to the following.

1) Differences in the initial guess fields of the microphysics. In the SC97 experiment, the rain mixing ratio for the whole model domain at the initial time of the assimilation period was known. Therefore, they were able to specify initial guess fields of the microphysics much closer to the simulation results. In the current experiment, the simulated observations are displaced over the whole volume scan and are projected onto the initial time to generate the initial guess. The misfit between the initial guess of the assimilation experiment and the simulation is therefore much greater than that in SC97's experiment; however, the current experimental design was much closer to the data collection strategy used for collecting data.

2) The current experiment has a relatively smaller amount of simulated observations and, therefore, a lower degree of overdetermination. In the SC97 experiments, two volume scans of radar observations were used for an assimilation period with 20 time steps of model integration. In the current experiment, the same number of observations are used for the assimilation period, but with 50 time steps. The longer assimilation period in this study also allows nonlinearities in the system to have greater impact.

The greater temperature perturbation value may also be noted. The temperature is diagnosed from the equation (without ice)

$$T = (p/p_0)^{R/C_P}\theta_{il}\left[1 + \frac{L_v}{C_P T}(q_c + q_r)\right].$$

None of the observations contain any information about temperature; the temperature has to be diagnosed from the dynamic and microphysical constraints on the system of equations.

### 2) MIXED-PHASE PHYSICS

In this experiment the model with the full microphysics (including ice phase) was used. The thick lines in Fig. 6 show the decline of the normalized cost function and gradient norm. When the decline of the cost function for the experiment with the ice phase included is compared to that without it, it can be noted that the effect of the inclusion reduced the rate of convergence. Contour plots of several variables are shown in Fig. 7 for the same time and cross section as shown in Fig. 5. Qualitatively the features are the same, but differences can be seen in the relative rms errors as shown in the second row of Table 1. As expected, the errors are larger than those from the previous experiment, but not by much. Therefore, it is concluded that the additional complexity introduced by the more complex ice microphysics has not resulted in a system with poor convergence properties.

### 3) STEADY-STATE EXPERIMENT

We also repeated the experiment by SC98 to investigate the effect of the assumption that the storm is steady during the period of observation, as is done in Doppler analysis. Since the storm advection speed is zero in the OSSE, all observations were projected to the same space position at the mean time of the volume scan. The relative rms errors of the retrieved fields are shown in Table 1. It is evident that both microphysics and dynamics retrievals are worse compared to those in which the time information was used.

## 5. Assimilation experiments

On 20 July 1986 three Doppler radars documented the evolution of an isolated thunderstorm in a weakly sheared environment over northern Alabama. The dominant cell of the cluster closely resembled the Byers and Braham model for warm-based, airmass storms (Byers and Braham 1949). This well-studied, relatively simple case provided a unique opportunity to test our new analysis algorithm.

The three radars started scanning the storm at 1306 central standard time (CST) in a coordinated manner and continued until well after the peak surface divergence was observed at 1325 CST. Each volume scan took about 3 min. Seven volume scans of the data were analyzed; these covered the cumulus, mature, and dissipation stages of the storm. During the cumulus stage (volume 1 from 1306 to 1309 CST, and volume 2 from 1309 to 1312 CST), the storm grew vigorously, and the cloud top rose about 6 km within 6 min. Ice phase particles began to grow during this stage. The reflectivity reached its maximum in volume 3 (from 1312 to 1315 CST) and subsequently began to descend (volume 4 from 1315 to 1317 CST). Heavy rain and pea-sized hail reached the surface (Tuttle et al. 1989). A reflectivity trench echo, caused by a midlevel downdraft, and a constriction at 9-km height were observed (KW91) in this stage. During the dissipation stage of the storm (volume 5 from 1317 to 1320 CST, volume 6 from 1320 to 1324 CST, and volume 7 from 1324 to 1327 CST), a strong microburst was observed.

All radar scans were edited in radar space before being interpolated to the model Cartesian space. Reflectivity and differential reflectivity were converted to gridpoint rain and ice mixing ratios using the procedure set forth in section 2 of the appendix. These mixing ratios and the observed radial velocities were fitted to the model-predicted quantities (radial velocities determined from the model wind components) using the volume scan time information, so that each measurement was compared to the model value at the time step closest to the actual observation.
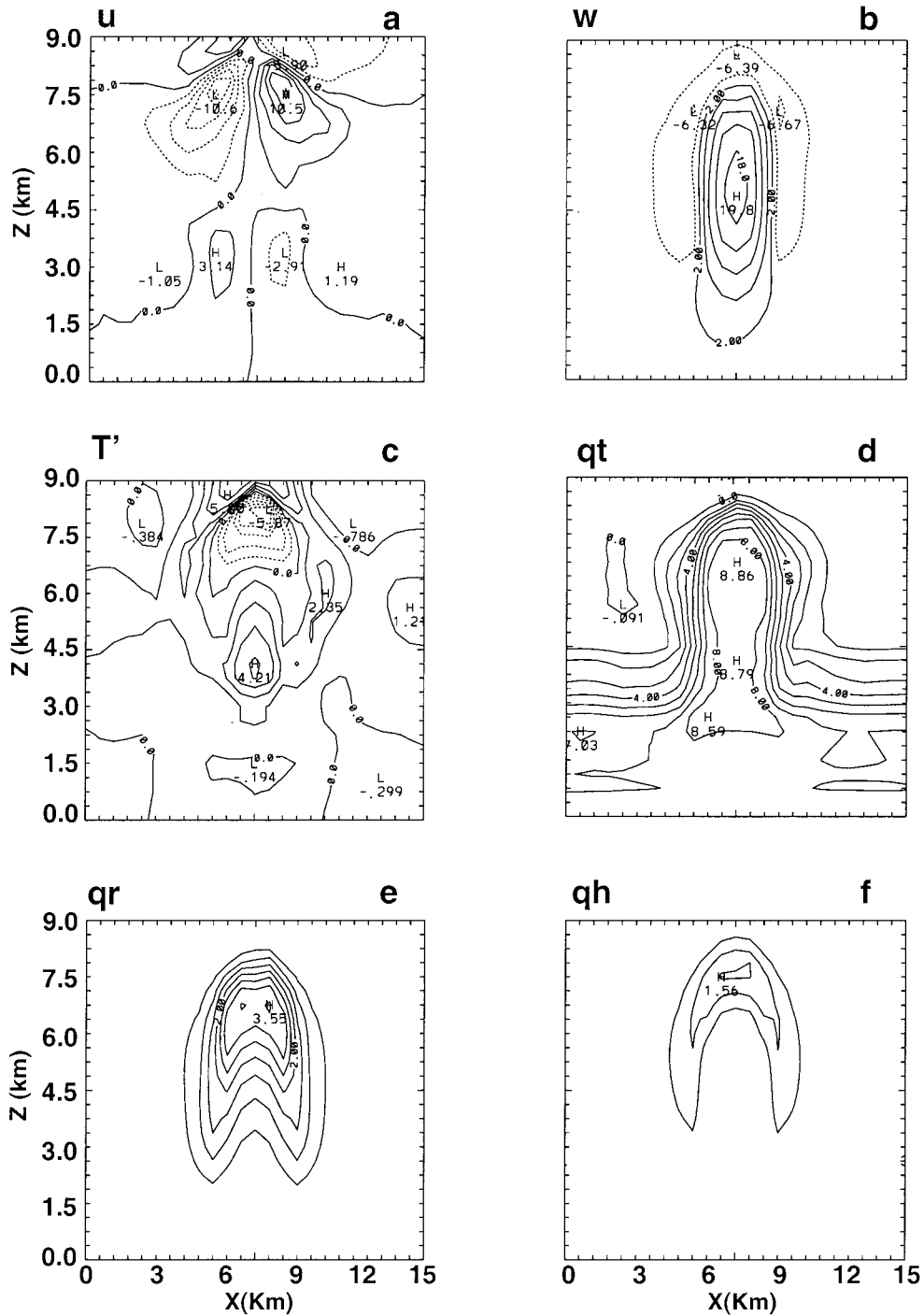
FIG. 7. Same as Fig. 5 but for the retrieved results.

Retrieval experiments for all sets of volume scans indicated that the model had converged to a solution consistent with the radar observations, with the best results obtained in the center of the assimilation period (this result is further discussed in a later section). Figure 8 shows the decline of the normalized cost function (dashed line) and gradient norm (solid line) with iter-

ation number for the retrieval using the set of volume scans from 1312 to 1317 CST (scans 3 and 4), which covers the mature stage of the storm. The cost function and gradient norm are reduced by more than 80% and 92%, respectively. These reductions are typical for all scans.

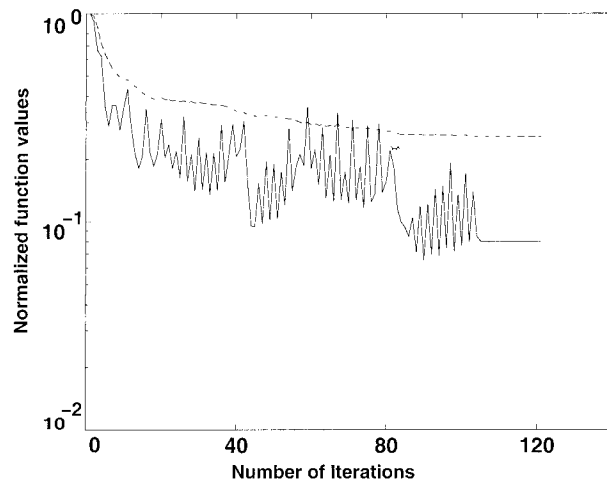Results at the end of each radar volume scan (close

FIG. 8. Normalized cost function (dashed line) and gradient norm (solid line) as a function of iteration numbers for the assimilation window of the mature stage (volume scans 3, 4).

to the middle of the each assimilation period) will be presented. These results are divided into the three stages of the storm evolution: cumulus, mature, and dissipation. The results are summarized by looking at time–height cross sections of the velocity fields.

*a. Cumulus stage*

The 20 July storm formed among several weaker cells. The analysis of KW91 revealed an actively growing new turret developing to the southwest of a decaying cloud. Figure 9 (the equivalent of the KW91 Fig. 4) shows horizontal cross sections at 7 km of reflectivity (Fig. 9a) and vertical velocity (Fig. 9b). The retrieval captured the decaying cell toward the northeast as well

as the vigorous growing cell in the southwest. The latter cell is the object of interest of these assimilation experiments. Upper-level divergence and environmental flow around this growing cell is evident at this level, close to cloud top, at this time. The growing cell consisted of a single boundary layer–rooted updraft in excess of 15 m s$^{-1}$, while the decaying cell was characterized by a weak downdraft. The positive temperature excess in the developing cell peaks at about 5 K at a height of 4.5 km. This value is higher than the maximum temperature excess of ~3 K retrieved by KW91, but is in agreement with the environmental sounding (Fig. 2), which shows a similar value for undiluted parcel ascent. The peaks in condensed water change with height above the surface from a peak of 4 g kg$^{-1}$ in cloud water at 4.5 km to a maximum of 7.5 g kg$^{-1}$ in rainwater at 6 km. At this stage in the cloud life cycle, graupel/hail was just being initiated; the maximum in graupel/hail content was 0.9 g kg$^{-1}$ at 8 km. This distribution of condensed water is consistent with the observed maximum and profile of the reflectivity fields.

Figure 10 shows the retrieved results at the end of the cumulus stage for the vertical cross section C–D in the Fig. 9. The cloud is now dominated by ice above 7.0 km. This glaciation resulted from the rapid freezing of rain and accretion of rain by graupel/hail above this level. The modeled cloud glaciation is consistent with $Z_{DR}$ radar observations (Tuttle et al. 1989). The $Z_{DR}$ values were close to zero above this level (indicative of ice phase particles), whereas below this level, $Z_{DR}$ was greater than 1.0 (indicative of big drops). The retrieved reflectivity maximum was at the height of 6.6 km with the value of around 60 dBZ, and corresponds to a mixed-phase region between the rainwater mixing ratio peak (8.9 g kg$^{-1}$ at 5.4 km) and the graupel/hail peak (2.4 g
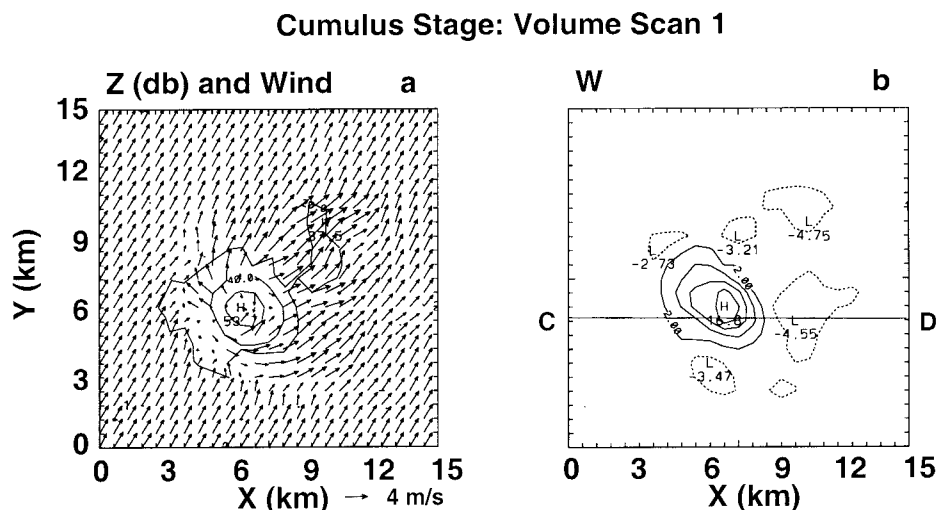
## Cumulus Stage: Volume Scan 1



FIG. 9. Horizontal cross sections of (a) reflectivity (contour interval is 10 dBZ) and wind vectors and (b) vertical velocity in m s$^{-1}$ (contour interval is 4 m s$^{-1}$) at the end of volume scan 1, 7 km above the ground. (b) The line CD represents the position of the vertical cross section for later figures.

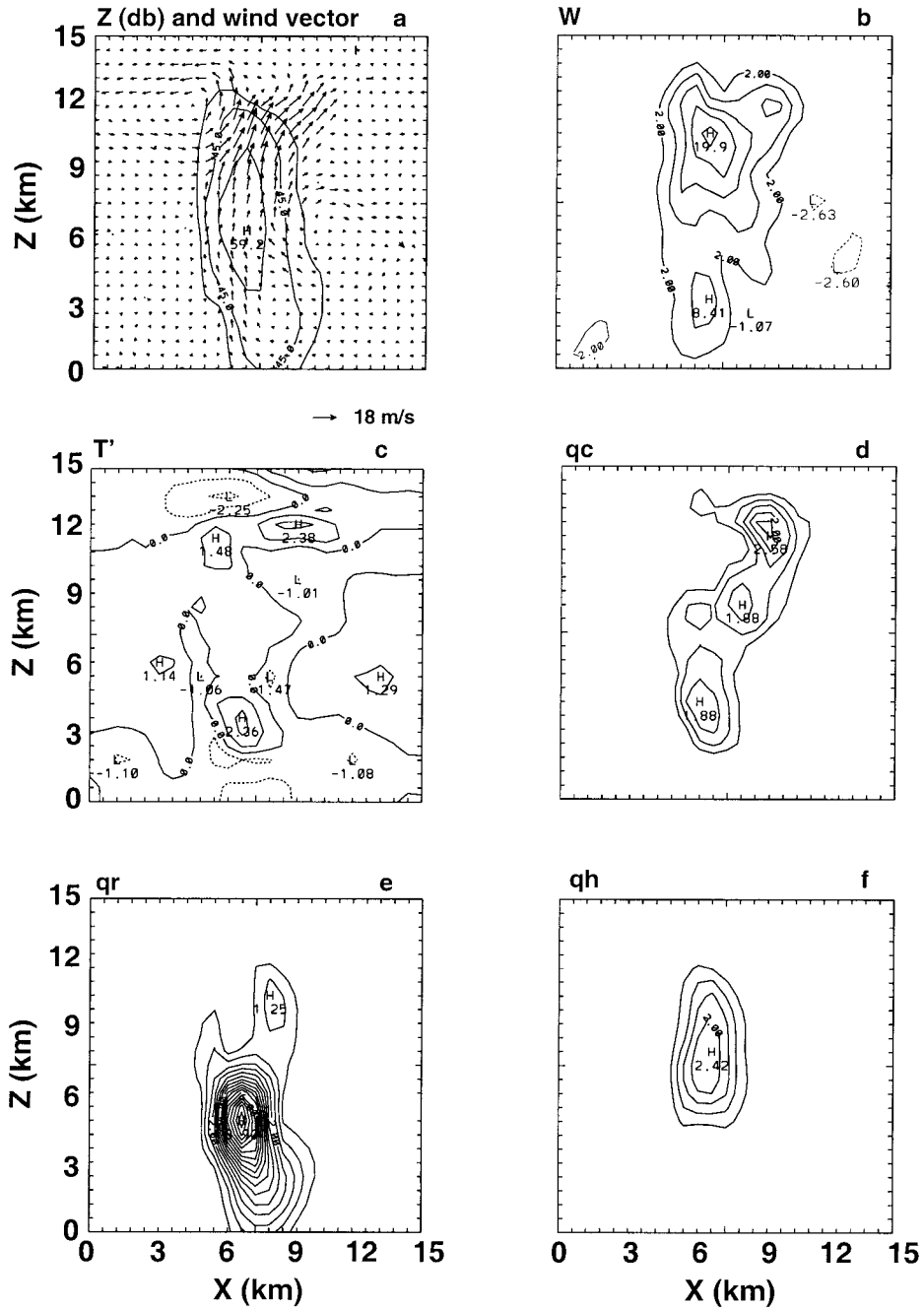**Cumulus Stage: Volume Scan 2**



FIG. 10. Vertical cross sections (along CD, Fig. 9) at the end of volume scan 2. Retrieved fields of (a) reflectivity (contour interval is 10 dBZ) and wind vector; (b) vertical velocity in m s$^{-1}$ (contour interval is 4 m s$^{-1}$); (c) temperature perturbation in °C (contour interval is 1°C); (d) cloud water mixing ratio (contour interval is 0.5 g kg$^{-1}$); (e) rainwater mixing ratio (contour interval is 0.5 g kg$^{-1}$); (f) graupel/hail mixing ratio (contour interval is 0.5 g kg$^{-1}$).

kg$^{-1}$ at 7.5 km). The observed reflectivity maximum was at a height of 7.2 km during this volume scan, which is approximately 600 m higher than the height of the retrieved reflectivity maximum. However, the observed

reflectivity maximum reached its peak height about 30 s before the time slice of Fig. 10. The observations indicate that the reflectivity maximum began to descend at about that time. For these reasons we attribute the

small discrepancy to the difference in sampling methods. The vertical cross section is an instantaneous view of the storm, whereas the radar samples the cloud sequentially.

It is also evident from Fig. 10 that the active growing cloud is characterized by positive temperature perturbations through its depth, with two temperature excess maxima. One of these maxima is at 12 km, associated with the freezing of ice in the growing cloud turret, while the other is at 3.5 km, slightly above the lifting condensation level. The value of the upper-level temperature excess remains below 3 K for this and all subsequent volume scans. In contrast, KW91 retrieved values in excess of ~6 K at upper levels for volume scans 2–4. They attributed this high value to the freezing of liquid water, stating that a reflectivity value $Z_e = 60$ dBZ would correspond to a liquid water content of ~15 g kg$^{-1}$ [using the $Z_e$–$q_r$ relationship of Hane and Ray (1985)], which would produce a temperature increase of ~5 K if frozen. However, our results indicate much lower condensed phase values, changing over a short period (3 min) from liquid to ice, which is consistent with the $Z_{DR}$ observations.

The low-level temperature excess maximum is associated with the condensation of lifted moist air from the surface. In all subsequent volume scans during the mature and even the dissipation stages of the cloud, this temperature excess was produced wherever there was evidence of air being lifted from the surface. The value of temperature excess has been reduced to ~3 K from the 5 K retrieved in volume scan 1. This reduction resulted from the evaporation of precipitation. These results differ from those reported by KW91, who found no temperature excess in volume scans 3 through 7. The observed cloud existed as the dominant cell in a small cluster. Radar observations indicated evidence of small cells trying to develop at its edges. The current retrieval analyzes a similar behavior. Note the temperature minimum below the level of free convection (LFC) and directly underneath the low-level temperature maximum in the updraft. This same pattern is repeated in all places where we observed low-level maxima in subsequent scans, which points to areas where new convective elements are being pushed through the LFC. Therefore, while differences in temperature fields between this and previous analyses were expected based on the results of the OSSE experiments, these results, though leading to different conclusions than the KW91 analysis, do present a physically consistent and plausible picture.

From Fig. 10 it is apparent that kinematic appearance of the thunderstorm during the cumulus stage resembles observed and modeled thermals. The cloud consisted of a single updraft, increasing in strength with height above the surface. As the cloud glaciated (going from volume 1 to volume 2), the updraft in the upper part accelerated, with some associated indications of midlevel entrainment at the base of the glaciation area as evidenced by the flow into the storm at 3.6 km (Fig. 10a).

### b. Mature stage

As the storm progressed from the cumulus to its mature stage, the retrieved vertical velocity reached a plateau at ~20 m s$^{-1}$ and then began to decrease to a value of ~12 m s$^{-1}$ at the transition to the dissipation stage. The precipitation core descended to a height of ~4 km and ~3.5 km at the end of volume scans 3 and 4, respectively. Precipitation reached the ground during volume 3, in agreement with the observations. The upper-level temperature excess gradually decreased and finally disappeared completely in the dissipation stage.

Figure 11 shows retrieved fields on the same horizontal cross section as in Fig. 10, but for the end of volume scan 4. The upper levels of the cloud are now mostly devoid of precipitation, and the hail core has descended to below the melting level. Cloud midlevels show indications of strong convergence and are characterized by a negative temperature perturbation.

KW91 identified two distinct features associated with the storm mature stage: the midlevel or cloud-edge downdraft (MLD), and a phenomena called ''constriction'' by Fujita and Black (1988). Constriction is a visible cloud feature that appears as though a belt has been tightened around the cloud. Both these features were captured in the current analysis (indicated by bold arrows in Figs. 10a,b).

Figure 12 shows reflectivity and vertical velocity contours for the 8-km horizontal cross section at the end of volume scan 4. This figure reveals two updraft maxima: one within the dominant cell, the other associated with the decaying cell to the northeast. In between these two updraft maxima is a downdraft at the down-shear edge of the dominant cell. The maximum speed retrieved in this downdraft is approximately 6 m s$^{-1}$. The magnitudes of both the updraft and downdraft in our analysis are lower than those in the KW91 analysis and the features are slightly shifted. However, the magnitude of the MLD is more in line with that in other storms (Knupp and Cotton 1987). In association with this midlevel downdraft, a weak reflectivity trench developed at the downshear side of the cloud. This can most clearly be seen in Fig. 11a, which reveals a distinct trench in the 35-dBZ contour on the downshear side of the storm.

KW91 hypothesized that the constriction phenomenon occurs when there is an acceleration of the vertical wind associated with the glaciation of the precipitation core, resulting in strong horizontal convergence at the midlevel in the cloud. However, our analyses indicate that the acceleration of the updraft was associated with the descent of the precipitation core, with its associated increase in buoyancy as the local water loading is reduced, as was hypothesized by Roberts and Wilson (1989). The cooler and drier environmental wind entrained into the cloud (as indicated by the velocity vectors on the southwest corner of the reflectivity cell in Fig. 12a) weakened the upper-level temperature excess maximum, and eroded the 35-dBZ reflectivity contour
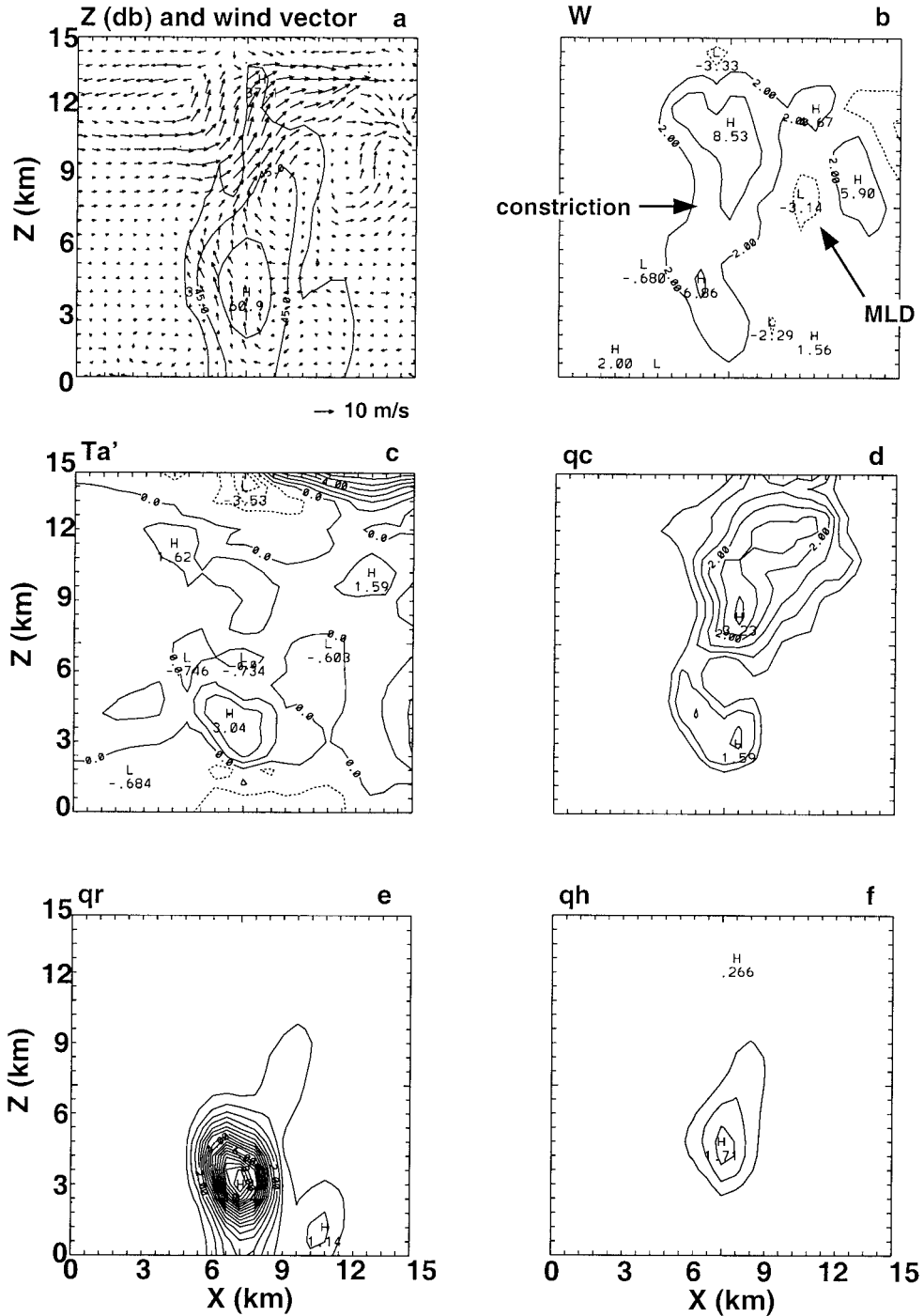
## Mature Stage: Volume Scan 4



FIG. 11. As Fig. 10 but for volume scan 4.

at the west side of the cloud between 8 and 9 km (indicated by arrows on Fig. 11).

During this part of the analysis there are noteworthy differences between our results and those of KW91. Their results indicated that winds between 9 and 14 km had an easterly component (negative $U$). However, in this analysis, the winds had a westerly component consistent with the environmental winds at those levels. The direction of the upper-level wind has a strong impact on the retrieval results. First, the midlevel inflow re-
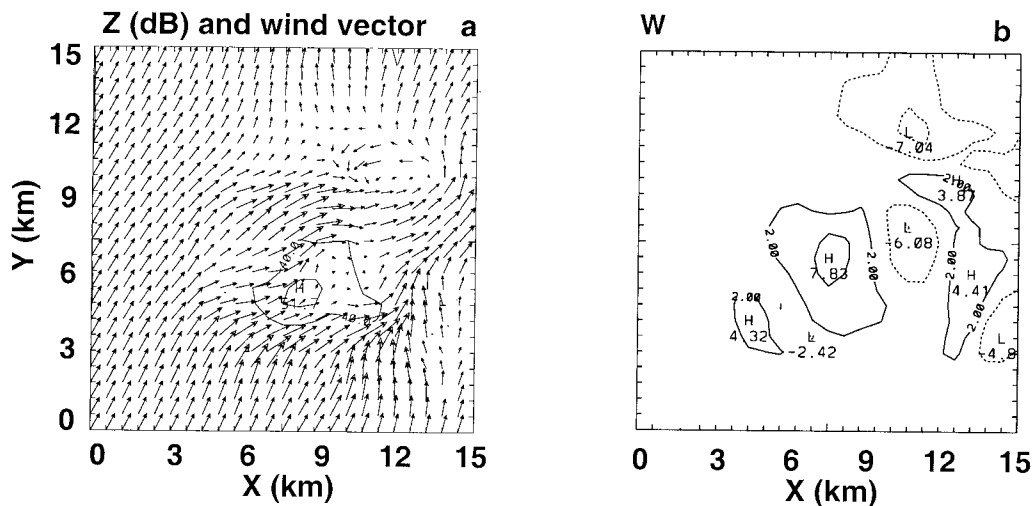
## Mature Stage: Volume Scan 4



FIG. 12. Horizontal cross sections of (a) reflectivity (contour interval is 10 dBZ) and wind vectors and (b) vertical velocity in m s$^{-1}$ (contour interval is 4 m s$^{-1}$) at the end of volume scan 1, 8 km above the ground.

sponsible for the constriction entered the storm from the southwest in this analysis (Fig. 12, southwest corner of reflectivity cell), as opposed to from the southeast, as KW91 had found. They felt it was difficult to explain because the environmental flow is coming from the southwest at this level. Second, when updraft air exits the easterly tilted updraft, it carries easterly momentum and continues flowing eastward. Since the environmental wind is from the southeast at this level ($\sim$13 km), there is strong convergence to the east of the cloud, resulting in a strong downdraft ($\sim$15 m s$^{-1}$). This downdraft is farther away from the cloud edge, is much stronger than the midlevel downdraft discussed above, and is very close to the eastern boundary of our model domain. In order to see if this was a boundary effect, we increased the model domain size (added 10 more grid points in both horizontal directions) and reran the analysis, with similar results. We attribute this downdraft to our forcing the model winds to relax to the environmental wind (horizontally uniform as determined from the environmental sounding, Fig. 2) for every grid point outside of the cloud and all times (SC97), thereby prohibiting the upper-level flow around the storm from responding to the intruding storm outflow air. This points out one of the major shortcomings of using only Doppler radar information, namely, the lack of observations in precipitation-free air.

To verify the correctness of the retrieval of the upper-level flows, we compared the observed radial velocity fields of all the radars to that which was calculated from the retrieved wind field and the terminal velocity of hydrometeor particles. Figure 13 shows a comparison for the precipitation-filled air for a vertical cross section through the CP4 data. The difference is mostly in that the retrieved pattern is smoother. The smoothness of the

retrieved values is consistent with the large gridpoint separation used in the model, which tends to smooth out small-scale inhomogeneities. Though not shown, the retrieved radial velocity also closely matched the radial velocity observations of radar CP2 and CP3.

### c. Dissipation stage

Since the storm was advected by the environmental wind during the observation period, it was necessary to move the model domain to the southeast during the dissipation stage. Therefore, the model domain was shifted 1.5 km to the south and 3.0 km to the east to accommodate this advection.

The retrieved fields in the vertical cross section through the core of the storm for volume scans 5 and 6 are shown in Fig. 14. These figures reveal the precipitation shaft at lower levels dominated by a strengthening downdraft. Upper-level winds reveal some continued upward motion on the upshear side of the storm (at $\sim$12 km), but by volume scan 6 most of what was the storm is characterized by downdraft. The condensed phase mixing ratios have been reduced by precipitation. Even though most of the graupel/hail has been melted while falling toward the surface, a maximum value of 0.2 g kg$^{-1}$ of graupel/hail has reached the surface.

The analysis retrieved a strong low-level downdraft at the time that the microburst was observed (Fig. 15a). The location of this downdraft ($\sim$13.5 km east of CP4 and 5.4 km north) corresponds well to the observed location of the microburst (KW91, Fig. 1; $\sim$12.7 km east and 6 km north). The maximum value of 7 m s$^{-1}$ is lower than the 13 m s$^{-1}$ analyzed by KW91 and the 14 m s$^{-1}$ modeled by Proctor (1989). However, this lower value is consistent with the vertical gridpoint sep-
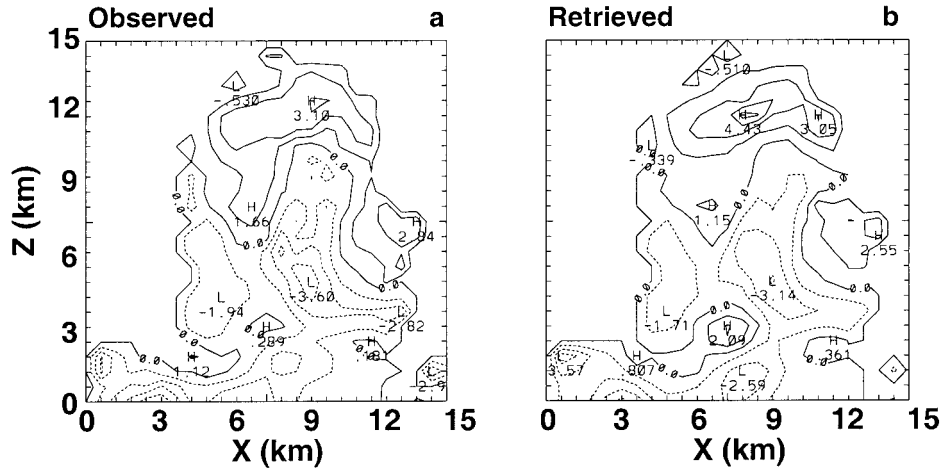
## Mature Stage: Volume Scan 4



FIG. 13. Vertical cross sections of CP4 radial velocities (m s$^{-1}$) for volume scan 4: (a) observed; (b) retrieved.

aration of 600 m used in our model. Proctor (1989) and Straka and Anderson (1993) suggested that a 600-m gridpoint separation may not be sufficient to capture the magnitude of microburst intensities in three-dimensional cloud models. A $-2$ K temperature perturbation in the lower cloud levels was retrieved in association with the incipient microburst. At the time of the microburst, lower cloud levels were characterized by strong convergence (Fig. 15b). The same sequence of events was analyzed by KW91.

### d. Overview of the storm

Time–height cross sections of maximum and minimum values of vertical velocity have been plotted in Fig. 16. Figure 16a shows that the updraft maximum ascended roughly 6 km within 9 min from volume scan 1 to volume scan 3, which is very close to the rise rate of the visible cloud top. The cloud reached its maximum updraft speed ($\sim$20 m s$^{-1}$) at the end of volume scan 2, and then began weakening. There is a trough of vertical velocity beginning in volume scan 3 at the height of 6.5 km, which follows the precipitation core (not shown in the figure). Just above this trough, there is a vertical velocity ridge representing the acceleration of the updraft after the precipitation core passed. KW91 analyzed the same general features, though magnitudes differed.

In Fig. 16b, the minimum values of midlevel vertical velocity from volume scan 3 to volume scan 7 are dominated by the downdraft close to the model domain boundary, as discussed in previous sections. This downdraft is initiated by the convergence at the 13-km height and is different from the downdraft analyzed by KW91. In their analysis the midlevel downdraft is much closer to the cloud. As discussed in previous sections, our an-

alyses retrieved a downdraft in a similar location, but of reduced magnitude.

The development of the low-level downburst is clearly captured in this analysis. The intense downdraft originated midway in volume 6 in the midcloud levels (associated with the melting of graupel/hail), and reached the surface toward the end of volume scan 7. The downburst is associated with the descent of the precipitation core.

### 6. Discussion

The primary goal of this study was to determine to what extent it is possible to obtain accurate dynamical and microphysical retrievals of a storm using a relatively simple microphysical parameterization. It was shown that we can successfully retrieve the major characteristics of the storm with these methods, and also that the microphysics fields found were consistent with the dynamics and the radar observations. However, all results that we show were constructed from only the first half of each assimilation period (see Fig. 4). When the second half of all the assimilation periods was evaluated, it was found that the storm weakened quickly, so that the updraft had weakened near the end of the assimilation period. This was the case for all volume scans, even during the cumulus stage.

The quick weakening of the storm in the case where the second half of the assimilation period was evaluated is illustrated by looking at the retrieved dynamics and microphysics fields in the mature stage of the storm evolution (Fig. 17). This figure represents the fields in the same cross section at the same time: the three left-hand panels are results from the center of the assimilation period, incorporating observations from volumes 3 and 4, while the three right-hand panels show the
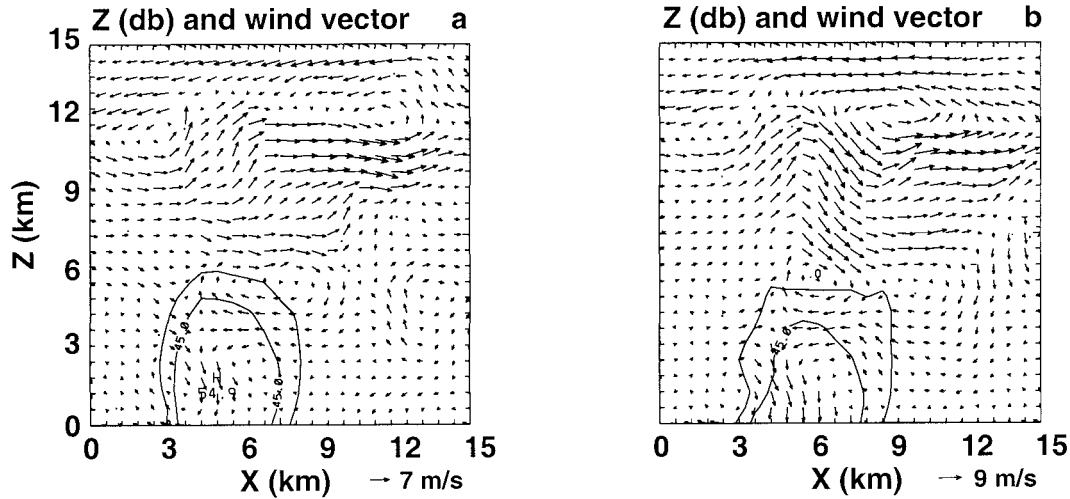
## Dissipating Stage: Volumes Scans 5 and 6



FIG. 14. Vertical cross sections through the core of the storm (Y = 4.8 km; see Fig. 15) of retrieved reflectivity and wind vectors for (a) volume scan 5 and (b) volume scan 6.

model fields at the end of the assimilation period for volumes 2 and 3 (see Fig. 4). Thus, the left-hand panels represent the storm structure as retrieved during the first half of each assimilation period, whereas the right-hand panels show the storm (for the same time) as retrieved at the end of the second half of the (different) assimilation period. The most obvious difference is the much weaker updraft in the right-hand panels, especially at upper levels. Furthermore, the magnitude of the reflectivity has been reduced by about 2 dB. This reflectivity reduction can be traced to a general decline in all the

condensed phase fields ($q_c$, $q_r$, $q_h$). All these are associated with a well-developed midlevel entrainment into the precipitation core. These matters were further explored.

Two possible explanations can be offered for the difficulty with the assimilation: 1) the model as formulated does not sufficiently describe the physics that determined the storm evolution in the observed dataset; or 2) the basic processes are so nonlinear that the 4DVAR assimilation approach, which inherently depends on linear approximations, is unable to adequately assimilate
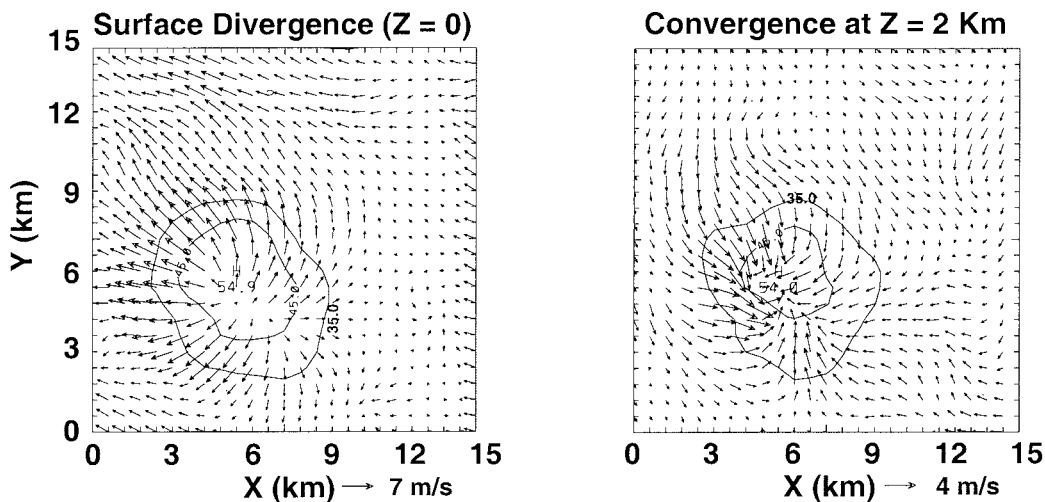
## Dissipating Stage: Volume 7



FIG. 15. Horizontal cross sections of retrieved reflectivity and wind vector fields at the end of the volume scan 7: (a) at the surface and (b) at 2 km.
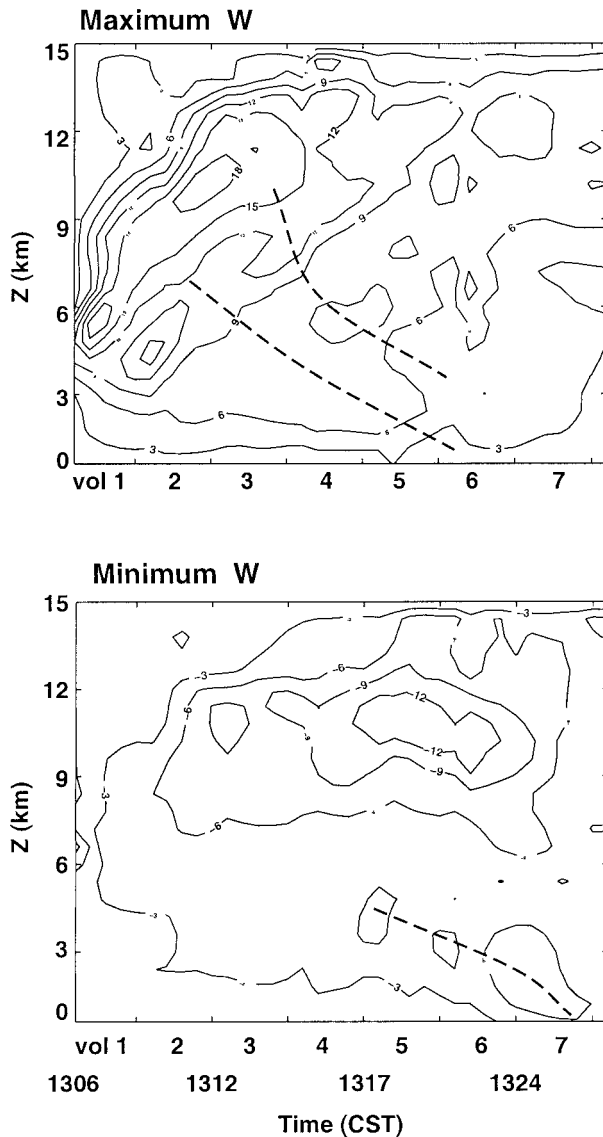
## Maximum W



## Minimum W



FIG. 16. Time–height cross section of vertical velocity: (a) maximum vertical velocity; (b) minimum vertical velocity.

the observations. Both options are discussed in the next two sections.

### a. Model inadequacies

Since we were able to adequately retrieve the model simulation in the OSSEs, indications are that the model physics are inadequate to describe the evolution of the real storm. The discussion in the previous section points to enhanced entrainment playing a role in the collapse of the storm. A close examination of the differences in the two assimilations (Fig. 17) reveals that all the condensed phase mixing ratios are substantially reduced. This reduction does not result from precipitation (since the precipitation core remains at approximately the same

location). Therefore, it has to come from evaporation. When comparing Fig. 17a to Fig. 17b, one notes that the cloud edges in Fig. 17b are all characterized by downdraft. The collective evidence then points to an overproductive mixing process, or to be specific, a diffusion coefficient, the value of which is too high. This diffusion coefficient was set to 150 m$^2$ s$^{-1}$, following the suggestion of SC97, and is the same as used in the OSSE, which gave reasonable results. However, when this value was lowered, it did not improve the assimilation. There was little impact at the middle of the assimilation period, but results at the end of the assimilation deteriorated. When the diffusion coefficient is set too low, inhomogeneities resulting from the adjoint technique begin to dominate the solution, since they are nonlinearly amplified. This then indicates that the model cannot adequately represent the evolution of the storm.

In addition to the above problem, we also found that the retrieval experiments were quite sensitive to several of the model microphysical parameters. In particular, it was sensitive to the parameter controlling the conversion of rain to ice [$A'$ in Eq. (A.5) in the appendix] and the intercept value of the hail distribution ($n_{0h}$). The impact of both of these parameters is related to their influence on the terminal fall velocity of hail. The biggest impact of condensed phase going to hail (as opposed to rain) is that it will fall faster, since it can attain larger sizes. Therefore, when rain is converted to hail, it is more effectively removed from the cloud, thus redistributing the water-loading effect in the cloud. The intercept value $n_{0h}$ effectively determines the mean diameter of the assumed exponential distribution, with lower $n_{0h}$ values corresponding to higher precipitation rates. The impact of both of these parameters was investigated.

The freezing of rain is the only process to initialize the ice phase in the model. This is modeled as being proportional to $\exp[A'(273.15 - T)] - 1$. The numerical simulations by Lin et al. (1983) suggest that the constant $A'$ should be around 0.6 K$^{-1}$ to have a reasonable ice-generating rate. Our OSSE experiments verified this. However, when this value was used for $A'$ in the assimilation experiments, the model became numerically unstable. This instability resulted from inhomogeneities in the initial conditions being amplified, causing the argument of the exponential function to attain large values. These large values then produced large freezing rates, which overdepleted the available rainwater content. Rather than limiting the transfer rates (which would introduce discontinuities) we opted to reduce the coefficient $A'$.

We used a value $A' = 0.55$ K$^{-1}$ for the OSSE experiments, while for the real assimilation experiments, we gradually reduced it from 0.45 K$^{-1}$ for the first assimilation period to 0.40 K$^{-1}$ for the second and 0.35 K$^{-1}$ for the remainder. These changes are consistent with the general trend of decreased importance of the process with the evolution of the storm (Lin et al. 1983). How-
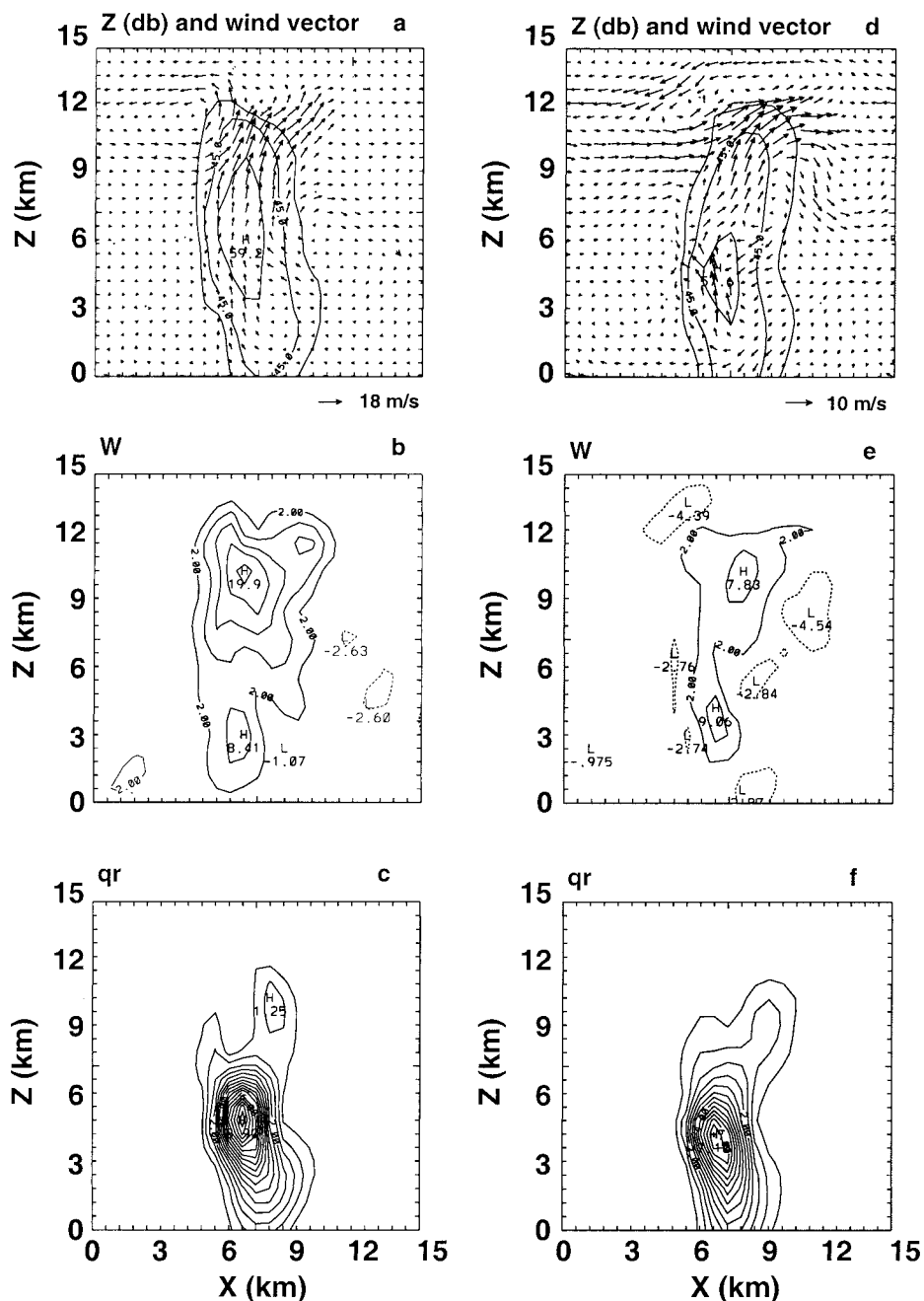
FIG. 17. Vertical cross sections of retrieved reflectivity and wind vectors (a), (d); vertical velocity (b), (e); and rainwater mixing ratios (c), (f); and the end of volume scan 3. (left) From the middle of the assimilation window when assimilating observations from volume scans 3 and 4; (right) from the end of the assimilation window when assimilating observations from volume scans 2 and 3.

ever, selection of these values were purely ad hoc, indicating that the parameterization does not capture the evolving physics of the storm.

The slope intercept value $n_{0h}$ impacts the fall velocity of hail directly. We increased its value from $4 \times 10^4$ $m^{-4}$ to $3 \times 10^5$ $m^{-4}$ as suggested by Straka and Anderson (1993). It produced good results early in the

simulation, but the lower fall speed impacted several of the dynamic features later in the storm. In particular, the midlevel downdraft became weaker, and the vertical velocity patterns in the mature stage were changed.

These results indicate the sensitivity of the retrieved dynamics to the modeled microphysics. Hence, the actual scheme chosen to parameterize the microphysics is
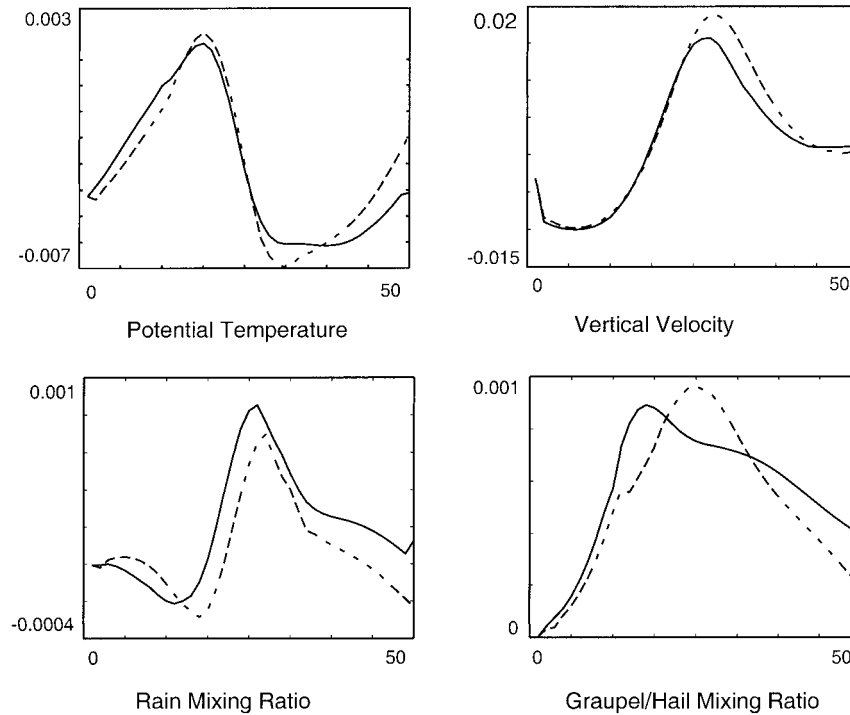
FIG. 18. Time evolution of the forward integrated error field values at a point close to the cloud edge (in the cloud). A 1% normalized random perturbation has been introduced to the initial fields. Dashed lines represents the nonlinear (NL) model and the solid line represents the TLM model.

important for the assimilation. The implication of this is that, whereas it may be possible to generate a reasonable looking storm in a forward simulation with a generic microphysical parameterization, these models may not be sufficient to assimilate observations of actual storms. This implication points to the need for parameter estimation to better adapt the microphysical (and dynamical) schemes for this problem. The optimal way to accomplish the parameter estimation would be to include the parameterization coefficients in the unknown of the optimization problem and solve for both the model initial fields and (possibly time varying) parameterization coefficients.

#### b. Nonlinear processes

With the increased complexity in the microphysical parameterization and the associated increase in discontinuously modeled processes, the question may be raised as to whether the model is sufficient for the application. The adjoint technique of data assimilation is inherently dependent on the linear approximation about a local state (Vukicevic and Errico 1993). We followed an approach similar to that of Vukicevic and Errico to test the suitability of the model. A tangent linear model (TLM) of the forward model was developed. Two simulations of the forward model were conducted, the second one being initiated with conditions slightly per-

turbed from those of the first (1% or less normalized random perturbations were introduced to the initial conditions). The TLM was integrated using the difference fields of the initial conditions in the two runs. The time evolution of the difference field between the two nonlinear fields were then compared to that of the TLM (Fig. 18, for a point within the cloud and close to the cloud edge). Results indicated that the full nonlinear model did not diverge away from the TLM solution over the period of integration.

These results indicated that the modeling system itself is consistent. However, it does not give any indication as to whether the model is sufficiently describing the nonlinearities of the actual atmospheric systems.

### 7. Conclusions

A 4DVAR data assimilation system, consisting of a three-dimensional time-dependent cloud model with both liquid and ice phase physics, has been developed to assimilate radar-observed measurements into the model. Initial observation system simulation experiments (OSSEs) indicated that the approach should be feasible. These OSSEs indicated that the steady-state assumption, frequently used to arrange individual radar volume scans, leads to degradation of results.

This system was then applied to the observational dataset of the 20 July 1986 thunderstorm from the Mi-

croburst and Severe Thunderstorm project database. Results were compared to the Doppler analysis of KW91. The assimilation system was able to retrieve all the major features of the storm analyzed by Kingsmill and Wakimoto, including the microburst, but there were also differences in details. In general, most of the vertical velocity features that the system produced were of lower magnitude. This lowering is likely related to the coarse resolution of the system (600-m gridpoint separation). Some differences were also noted in the temperature perturbation fields. However, the OSSEs have shown that the system has an inherent weakness in retrieving the temperature fields.

Even though the above results look reasonable, there are some areas of concern. In particular, the model was unable the accurately follow the evolution of the observed storm, even for the relatively short assimilation period of ~6 min. During the first half of each assimilation period, the model tracked the observed evolution of the storm well. However, in the second half the retrieved storm rapidly departed from the observed evolution, indicating that the model physics was unable to follow the actual cloud physics. The model results were sensitive to certain coefficients of the microphysical parameterization, and the simple mixing parameterization used was inadequate for the task. These problems indicate that while simple microphysical parameterizations may produce reasonable simulated clouds, it may not be sufficient to describe the real cloud processes, therefore suggesting the need for parameter estimation based on observations.

Tests were also performed to evaluate the impact of model nonlinearities on the retrieval process. These tests indicated that the the model should be able to perform the assimilation process, a result further confirmed by the OSSE experiments. The inability of the model to follow the observed evolution then suggests that the model may not be describing accurately the actual nonlinear processes in the atmosphere.

## APPENDIX

### Ice Microphysics

#### a. Processes

The microphysical parameterization used in this modeling system is an extension of that reported by SC97. Only processes related to the graupel/hail are described here. The parameterization schemes are based on the work of Orville and Kopp (1977) and Lin et al. (1983). The liquid phase physics was documented by Sun and Crook (1997). We will use notations that are consistent with those used by Sun and Crook.

Both rain and graupel are assumed to be distributed in size according to an exponential distribution given by

$$f(D) = \frac{1}{D_m} \exp\left(-\frac{D}{D_m}\right), \quad (A.1)$$

where

$$D_m = \left(\frac{\rho_a q}{\pi \rho n_0}\right)^{1/4} \quad (A.2)$$

is the mean diameter of the hydrometeor particles, $q$ is the mixing ratio, $\rho$ is the mass density of the hydrometeor, and $\rho_a$ is mass density of air. The constant $n_0$ is $4 \times 10^4$ m$^{-4}$ for graupel, and $8 \times 10^6$ m$^{-4}$ for rain.

We use the mass-weighted terminal velocity, given by

$$V_{Tm} = \left(\frac{4\rho g}{3\rho_a C_D}\right)^{1/2} \frac{\Gamma\left(3 + \frac{1}{2} + 1\right)}{\Gamma(3 + 1)} D_m^{1/2}, \quad (A.3)$$

to represent the mean fall velocity of the distribution. Here $C_D = 0.6$ is the drag coefficient.

The conservation equation of the graupel is

$$\frac{d\rho_a q_h}{dt} = R_{HFR} + R_{HAC} + R_{HAR} + R_M + \frac{\rho_a d(q_h V_{Tmh})}{dz}$$

$$+ k_w \nabla^2 \rho_a q_h, \quad (A.4)$$

where the $R_x$ terms are source and sink terms given by the following.

1) The production rate of graupel through rainwater freezing is

$$R_{HFR} = 20\pi^2 B' n_{0r} \rho_w D_{mr}^7 \{\exp[A'(T_0 - T)] - 1\}, \quad (A.5)$$

where $\rho_w$ is mass density of liquid water, $A' = 0.35$ K$^{-1}$ and $B' = 100$ m$^{-3}$ s$^{-1}$ are constants, and $T$ and $T_0 = 273.15$ K are the temperatures.

2) The production rate of graupel through accretion of cloud water is

$$R_{HAC} = \frac{\pi n_{0h} \rho_a \Gamma(3.5) E q_c}{4} \left(\frac{4g\rho_h}{3\rho_a C_D}\right)^{1/2} D_{mh}^{3.5}, \quad (A.6)$$

where $E$ is the collection efficiency of graupel for cloud water. We set $E = 1$ in our model.

3) The production rate of graupel through accretion of rain drops is

$$R_{HAR} = E\pi^2 \rho_w n_{0h} n_{0r} |V_{Tmr} - V_{Tmh}|$$

$$\times (5D_{mr}^6 D_{mh} + 2D_{mr}^5 D_{mh}^2 + 0.5D_{mr}^4 D_{mh}^3), \quad (A.7)$$

where $E = 1$ now is the collection efficiency of graupel for rainwater, and $V_{Tmr}$ and $V_{Tmh}$ are the mass-weighted terminal velocities for rain and graupel, respectively.

4) The sink term for the melting graupel is given by

$$R_M = -\frac{2\pi n_{0h}}{L_f}[K_a(T - T_0) + L_v\psi\rho_a(q_v - q_{v0})]$$

$$\times\left[0.3\Gamma(2.75)D_{mh}^{2.75}\nu^{-0.5}\left(\frac{4g\rho_h}{3\rho_a C_D}\right)^{0.25} + 1.6D_{mh}^2\right]$$

$$-\frac{C_W}{L_f}(T - T_0)\left(\frac{4R_{HAC}}{\pi} + R_{HAR}\right),\quad (A.8)$$

where $L_f$ and $L_v$ are the latent heats of fusion and vaporization, $K_a$ is the thermal conductivity of air, $\psi$ is the diffusivity of water vapor in the air, $q_v$ is the ambient vapor mixing ratio, $q_{v0}$ is the saturation mixing ratio at $T_0$, $\nu = \eta/\rho_a$ is the kinematic viscosity of air, $\eta$ is the dynamics viscosity of air, and $C_W$ is the specific heat of water. Melting only happens when environmental temperatures are higher than melting temperature $T_0 = 273.15$ K. Four mechanisms that supply the heat required to melt graupel have been considered: conduction of heat from the environmental air, transfer of latent heat by the condensation of water vapor on the graupel, and accretion of cloud water and rainwater when temperatures are larger than $T_0$.

The last two terms in the conservation equation represent precipitation and diffusion.

The ice–liquid potential temperature (Tripoli and Cotton 1981) was used as the prognostic temperature variable in the model. The thermodynamics equation is then, with the addition of a diffusion term,

$$\frac{d\rho_a\theta_{il}}{dt} = \frac{\rho_a\theta_{il}^2}{C_P T\theta}\left[L_v\frac{d(q_h V_{Tmh})}{dz} + L_s\frac{d(q_r V_{Tmr})}{dz}\right]$$

$$+ k\nabla^2\rho_a\theta_{il},\quad (A.9)$$

where $\theta_{il}$ is the ice–liquid–vapor potential temperature, $L_s$ is the latent heat of sublimation, and $k$ is diffusivity of $\theta_{il}$.

The temperature and cloud water mixing ratio are diagnosed from the prognostic variables, by assuming that all vapor in excess of the saturation value is converted to cloud water. Their relationship is

$$T = (p/p_0)^{R/C_P}\theta_{il}\left[1 + \frac{L_v}{C_P T}(q_c + q_r) + \frac{L_s q_h}{C_P T}\right]\quad (A.10)$$

and

$$q_c = \begin{cases}(q_t - q_r - q_h - q_{vs}) & \text{if } (q_v \geq q_{vs})\\ 0 & \text{if } (q_v < q_{vs}).\end{cases}\quad (A.11)$$

The saturation mixing ratio $q_{vs}$ is given by the saturation mixing ratio over water:

$$q_{vs} = \frac{3.8}{p}\exp\left(\frac{17.27(T - 273.16)}{T - 35.86}\right).\quad (A.12)$$

### b. Method to use differential reflectivity $Z_{DR}$

We calculate radar reflectivity at horizontal and vertical polarization for the raindrops or the graupel following Brandes et al. (1995):

$$Z_{Hrain} = \frac{n_{0r}}{V_s}\int D^6 \exp\left(-\frac{D}{D_{mr}}\right)dD\quad (A.13)$$

$$Z_{Vrain} = \frac{n_{0r}}{V_s}\int D^6(1.03 - 0.062D)^{7/3}\exp\left(-\frac{D}{D_{mr}}\right)dD\quad (A.14)$$

$$Z_{Hice} = \frac{n_{0h}}{5.28V_s}\int D^6 \exp\left(-\frac{D}{D_{mh}}\right)dD,\quad (A.15)$$

where $V_s$ the sampling volume. With this partitioning of liquid rain and ice particles, the differential reflectivity can be inferred from

$$Z_{DR} = 10 \log\frac{Z_{Hrain} + Z_{ice}}{Z_{Vrain} + Z_{ice}}.\quad (A.16)$$

(All of the above reflectivities are expressed in units of mm$^6$ m$^{-3}$.)

The Newton–Raphson method (Press et al. 1992) has been used to diagnose the liquid rainwater content ($q_r$) and graupel/hail ($q_h$) from the above equation and

$$10 \log(Z_S) = 10 \log(Z_{Hrain} + Z_{ice}),\quad (A.17)$$

where both $Z_{DR}$ and $Z_S$ are from radar observations.

The terminal velocity incorporated in the model is reflectivity weighted:

$$V_{Tm} = \frac{Z_{Hrain}V_{Tmr} + Z_{ice}V_{Tmh}}{Z_{Hrain} + Z_{ice}}.\quad (A.18)$$

### REFERENCES

Brandes, E. A., J. Vivekanandan, J. D. Tuttle, and C. J. Kessinger, 1995: A study of thunderstorm microphysics with multiparameter radar and aircraft observations. *Mon. Wea. Rev.,* **123,** 3129–3143.

Bringi, V. N., and A. Hendry, 1990: Technology of polarization diversity radars in meteorology. *Radar in Meteorology,* D. Atlas, Ed., Amer. Meteor. Soc., 153–190.

Byers, H. R., and R. R. Braham Jr., 1949: *The Thunderstorm.* U.S. Government Printing Office, 287 pp. [Available from U.S. Government Printing Office, Washington, DC 20402.]

Dodge, J., J. Arnold, G. Wilson, J. Evans, and T. T. Fujita, 1986: The Cooperative Huntsville Meteorological Experiment (COHMEX). *Bull. Amer. Meteor. Sci.,* **67,** 417–419.

Fujita, T. T., and P. G. Black, 1988: Monrovia microburst of 20 July 1986: A study of ''SST.'' Preprints, *15th Conf. on Severe Local Storms,* Baltimore, MD, Amer. Meteor. Soc., 380–383.

Gal-Chen, T., 1978: A method for the initialization of the anelastic equations: Implications for matching models with observations. *Mon. Wea. Rev.,* **106,** 587–606.

Hane, C. E., and P. S. Ray, 1985: Pressure and buoyancy fields derived from Doppler radar data in a tornadic thunderstorm. *J. Atmos. Sci.,* **42,** 18–35.

Hauser, D., F. Roux, and P. Amayenc, 1988: Comparison of two methods for the retrieval of thermodynamic and microphysical variables from Doppler radar measurements: Application to the case of a tropical squall line. *J. Atmos. Sci.,* **45,** 1285–1303.

Jameson, A. R., and D. B. Johnson, 1990: Cloud microphysics and radar. *Radar in Meteorology,* D. Atlas, Ed., Amer. Meteor. Soc., 323–340.

Kapitza, H., 1991: Numerical experiments with the adjoint of a non-hydrostatic mesoscale model. *Mon. Wea. Rev.,* **119,** 2993–3011.

Kingsmill, D. E., and R. M. Wakimoto, 1991: Kinematic, dynamic, and thermodynamic analysis of a weakly sheared severe thunderstorm over northern Alabama. *Mon. Wea. Rev.,* **119,** 262–297.

Knupp, K. R., and W. R. Cotton, 1987: Internal structure of a small mesoscale convective system. *Mon. Wea. Rev.,* **115,** 629–645.

Laroche, S., and I. Zawadzki, 1994: A variational analysis method for retrieval of three-dimensional wind field from single-Doppler radar data. *J. Atmos. Sci.,* **51,** 2664–2684.

Lewis, J. M., and J. C. Derber, 1985: The use of adjoint equations to solve a variational adjustment problem with advective constraints. *Tellus,* **37A,** 309–322.

Lin, Y.-L., R. D. Farley, and H. D. Orville, 1983: Bulk parameterization of the snow field in a cloud model. *J. Climate Appl. Meteor.,* **22,** 1065–1089.

Liu, D. C., and J. Nocedal, 1989: On the limited memory BFGS method for large-scale optimization. *Math. Programming,* **45,** 503–528.

Navon, I. M., X. Zou, J. Derber, and J. Sela, 1992: Variational data assimilation with an adiabatic version of the NMC spectral model. *Mon. Wea. Rev.,* **120,** 1433–1446.

Orville, H. D., and F. J. Kopp, 1977: Numerical simulation of the life history of a hailstorm. *J. Atmos. Sci.,* **34,** 1596–1618.

Press, W. H., S. A. Teukolsky, W. T. Vetterling, and B. P. Flannery, 1992: *Numerical Recipes in Fortran 77: The Art of Scientific Computing.* Cambridge University Press, 933 pp.

Proctor, F. H., 1989: Numerical simulations of an isolated microburst. Part II: Sensitivity experiments. *J. Atmos. Sci.,* **46,** 2143–2165.

Qiu, C.-J., and Q. Xu, 1992: A simple adjoint method of wind analysis for single-Doppler data. *J. Atmos. Oceanic Technol.,* **9,** 588–598.

Roberts, R. D., and J. W. Wilson, 1989: A proposed microburst nowcasting procedure using single-Doppler radar. *J. Appl. Meteor.,* **28,** 285–303.

Seliga, T. A., K. Aydin, and H. Direskeneli, 1986: Disdrometer measurements during an intense rainfall event in central Illinois: Implications for differential reflectivity radar observations. *J. Climate Appl. Meteor.,* **25,** 835–846.

Shapiro, A., S. Ellis, and J. Shaw, 1995: Single-Doppler velocity retrievals with Phoenix II data: Clear air and microburst wind retrievals in the planetary boundary layer. *J. Atmos. Sci.,* **52,** 1265–1287.

Straka, J. M., and J. R. Anderson, 1993: Numerical simulations of microburst-producing storms: Some results from storms observed during COHMEX. *J. Atmos. Sci.,* **50,** 1329–1348.

Sun, J., and A. Crook, 1994: Wind and thermodynamic retrieval from single-Doppler measurements of a gust front observed during Phoenix II. *Mon. Wea. Rev.,* **122,** 1075–1091.

——, and ——, 1997: Dynamical and microphysical retrieval from Doppler radar observations using a cloud model and its adjoint. Part I: Model development and simulated data experiments. *J. Atmos. Sci.,* **54,** 1642–1661.

——, and ——, 1998: Dynamical and microphysical retrieval from Doppler radar observations using a cloud model and its adjoint. Part II: Retrieval experiments of an observed Florida convective storm. *J. Atmos. Sci.,* **55,** 835–852.

——, D. Flicker, and D. Lilly, 1991: Recovery of three-dimensional wind and temperature fields from simulated single-Doppler radar data. *J. Atmos. Sci,* **48,** 876–890.

Talagrand, O., and P. Courtier, 1987: Variational assimilation of meteorological observations with the adjoint vorticity equation. I: Theory. *Quart. J. Roy. Meteor. Soc.,* **113,** 1311–1328.

Tripoli, G. J., and W. R. Cotton, 1981: The use of ice–liquid water potential temperature as a thermodynamic variable in deep atmospheric models. *Mon. Wea. Rev.,* **109,** 1094–1102.

Tuttle, J. D., V. N. Bringi, H. D. Orville, and F. J. Kopp, 1989: Multiparameter radar study of a microburst: Comparisons with model results. *J. Atmos. Sci.,* **46,** 601–620.

Verlinde, J., and W. R. Cotton, 1993: Fitting microphysical observations of nonsteady convective clouds to a numerical model: An application of the adjoint technique of data assimilation to a kinematic model. *Mon. Wea. Rev.,* **121,** 2776–2793.

Vivekanandan, J., R. Raghavan, and V. N. Bringi, 1993: Polimetric radar modeling of mixtures of precipitation particles. *IEEE Trans. Geosci. Remote Sens.,* **31,** 1017–1034.

Vukicevic, T., and R. M. Errico, 1993: Linearization and adjoint of parameterized moist diabatic processes. *Tellus,* **45A,** 493–510.

Wakimoto, R. M., and V. N. Bringi, 1988: Dual-polarization observations of microbursts associated with intense convection: The 20 July storm during the MIST project. *Mon. Wea. Rev.,* **116,** 1521–1539.

Wolfsberg, D. G., 1987: Retrieval of three-dimensional wind and temperature fields from single-Doppler radar data. Ph.D. thesis, University of Oklahoma, 91 pp. [Available from Cooperative Institute for Mesoscale Meteorological Studies, 815 Jenkins, Norman, OK 73019.]

Xu, Q., 1996: Generalized adjoint for physical processes with parameterized discontinuities. Part I: Basic issues and heuristic examples. *J. Atmos. Sci.,* **53,** 1123–1142.